Automatic indexing of two-dimensional patterns in reciprocal space

Josef Simbrunner [1,*] Jari Domke [2,*] Falko Sojka [2] Daniel Knez [3] Roland Resel [4]
Torsten Fritz [2] and Roman Forker [2,†]

[1]*Division of Neuroradiology, Vascular and Interventional Radiology, Medical University Graz, Auenbruggerplatz 9, Graz 8036, Austria*
[2]*Institute of Solid State Physics, Friedrich Schiller University Jena, Helmholtzweg 5, Jena 07743, Germany*
[3]*Institute of Electron Microscopy and Nanoanalysis, Graz University of Technology, Steyrergasse 17/III, Graz 8010, Austria*
[4]*Institute of Solid State Physics, Graz University of Technology, Petersgasse 16, Graz 8010, Austria*

An indispensable part of the structure determination of crystalline two-dimensional (2D) materials and epitaxial thin films is the correct indexing of the acquired diffraction patterns. In our previous work, we described an effective algorithm to determine the 3D unit-cell parameters of complex systems comprising different orientations and polymorphs. In this work, we adapt the indexing method to 2D lattices in reciprocal space. Analyzing low-energy electron diffraction and Fourier-transformed scanning tunneling microscopy measurements, the method is exemplarily applied to thin films of conjugated molecules like 3,4:9,10-perylenetetracarboxylic dianhydride (PTCDA), 6,13-pentacenequinone (P2O), and vanadyl phthalocyanine (VOPc) grown by physical vapor deposition on Ag(111). In all cases unit cells (rhomboids) along with their sixfold rotationally or mirror symmetric counterparts are determined. The already known commensurate epitaxial relationship is reproduced for PTCDA on Ag(111), demonstrating the validity of our method. In the case of P2O/Ag(111) a point-on-line epitaxial condition is found. Our algorithm can be equally well applied to all kinds of 2D patterns in reciprocal space where a crystallographic indexing is required, e.g., electron diffraction data [such as transmission electron diffraction, selected area electron diffraction (SAED)] and fast Fourier transforms (FFTs) of scanning probe images. To demonstrate this aspect, we evaluate FFTs of scanning tunneling microscopy data for stacked VOPc/PTCDA heteroepitaxial layers on Ag(111) as well as SAED data of an epitaxial TiO_2/LaAlO$_3$(100) heterostructure in cross section.

I. INTRODUCTION

Crystal structure identification of both thin organic and inorganic films, especially two-dimensional (2D) materials beyond graphene, attracts considerable interest, amongst others, in potential electronic applications and pharmaceutical science [1–10]. The presence of a single crystalline substrate surface during the crystallization process can induce new types of molecular or atomic packing because the substrate tends to act as a template for the crystallization process. This becomes especially severe in cases where the respective bulk crystal does not contain lattice planes in which the molecules lie (almost) flat. In such cases, often a substrate-induced growth is observed, where the first monolayer is characterized by molecules lying flat on the surface [11–16]. Further, if molecular crystals are epitaxially grown on single-crystalline substrates, multiple preferred orientations of the adsorbate, several symmetry-related in-plane alignments, and the emergence of unknown polymorphs can occur [17–20]. For inorganic epitaxial layers also unknown surface-induced polymorphs are frequently observed, such as the formation of a 2D network consisting of so-called blue phosphorene and gold linker atoms [8] or the growth of a strained silicene monolayer on Au(111) [9].

Crystal structure solutions from thin films are often performed by x-ray diffraction (XRD) experiments. The analysis of such diffraction patterns relies on the indexing of the obtained reflexes to determine the reduced unit cells of the crystallographic lattice. For 3D patterns, a manifold of algorithms and automatic software packages exist, mainly tailored to single crystal diffraction [21–25]. In previous work, we described an algorithm that proved effective for thin film analysis, where unit cells in various orientations and/or with different lattice parameters were analyzed [16,26].

For studying epitaxial growth, the molecular or atomic layers and their relation to the substrate has gained special interest [27]. For this purpose, surface-sensitive methods, such as low-energy electron diffraction (LEED) and scanning tunneling microscopy (STM), are especially suited when the first monolayer (contact layer) is of interest, while x-ray based methods typically require a larger volume of scattering material.

LEED experiments use a collimated electron beam incident on the sample. Because of the low energy of the electrons (typically 20–200 eV), the electrons only penetrate a few atomic layers into the sample [28,29] and are scattered mostly elastically by the surface atoms (nonelastically scattered electrons can be filtered out by special grids). Therefore, the diffraction pattern depends only on the 2D crystal structure of the sample,

---

*These authors contributed equally to this work.
†Corresponding author: roman.forker@uni-jena.de

containing diffraction reflexes from both the adlayer and the single crystalline substrate surface in the case of thin films of only a few monolayers in thickness. The intensities of the various diffracted beams can, in principle, be recorded as a function of the incident electron beam energy to generate so-called I-V curves (also known as dynamical LEED [30,31]), which, by comparison with theoretical curves, may provide accurate information on atomic positions. However, dynamic scattering calculations usually require periodic boundary conditions (and are hence tailored to commensurate registries) [8,32], because noncommensurate epitaxial relations imply an unmanageable number of different multiple scattering paths. Yet, applying geometrical LEED theory, the analysis of the spot positions yields valuable information on the size, symmetry, and rotational alignment of the adsorbate unit cell with respect to the substrate unit cell, and is further able to include multiple scattering effects. In the case of distortion-corrected LEED which we generally apply here, those lattice parameters can be determined with high precision (accuracy of measured lattice constants $\approx 1\%$ or better) [33,34]. However, geometrical LEED analysis is not sufficient to unequivocally deduce the content of the unit cell which often comprises several atoms and/or molecules. Therefore, an insightful structural analysis of ultrathin molecular films requires the combination of reciprocal space methods (LEED, electron diffraction in electron microscopy, XRD) and real space methods, favorably in the form of scanning probe techniques. STM or atomic force microscopy (AFM) performed with functionalized tips provide images of solid surfaces with molecular or even atomic resolution and allow for an unambiguous elucidation of the unit cell content [35–37]. On the downside, it is almost impossible to calibrate such apparatuses to the required lateral precision of 1% or better. Yet, as we and others have shown in the literature [14,38–41], this limitation can be circumvented by analyzing the fast Fourier transform (FFT) of said images. Then, either the FFT contains reflexes of the *a priori* known substrate surface which allow for an *a posteriori* calibration of the image, or the FFT can be scaled by means of a LEED image of the same sample. The first case is especially valuable when the sample contains only small domains of different polymorphs simultaneously, such that LEED does not yield conclusive results. Nevertheless, in both cases an indexing of the FFT is highly beneficial.

Yet another very important experimental method for characterizing lattice alignment is transmission electron diffraction (TED), often performed in the variant of selected area electron diffraction (SAED) within a transmission electron microscope (TEM), operated with an electron energy of 100–300 keV. This technique proved to be especially useful for the site-specific analysis of crystalline materials [42,43]. Compared to LEED, the results are similar insofar as a direct image of the reciprocal space is obtained. However, TED and SAED typically suffer much less from image distortions than LEED.

In this work, we adapt our previously described algorithm for indexing grazing incidence x-ray diffraction (GIXD) patterns [26] to 2D reciprocal patterns. The usual approach to indexing 2D reciprocal lattices relies heavily on educated guesses, trial and error, as well as the intuition and experience
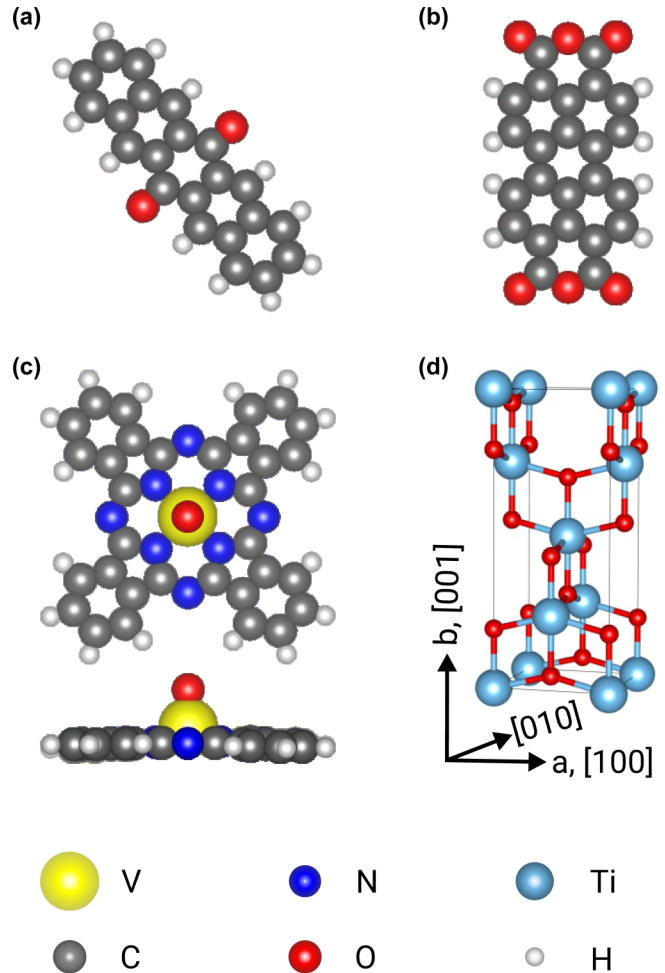

FIG. 1. Substances used as adlayers in this work. (a) P2O, (b) PTCDA, (c) VOPc (top view and side view), (d) TiO$_2$ (anatase). The color code of the atoms is displayed in the legend.

of the experimenter, which we attempt to replace by a more systematic and less subjective approach. For this purpose, potential solutions within certain boundary conditions are tested. While, in principle, those can be chosen loosely to allow for a more extensive screening, they are necessary in practice to reduce computational costs to a reasonable level as well as to rule out unit cells that are of unrealistic size.

Our method is exemplarily applied to LEED patterns of monolayers of conjugated molecules like 3,4:9,10-perylenetetracarboxylic dianhydride (PTCDA, CAS No.: 128-69-8) and 6,13-pentacenequinone (P2O, CAS No.: 3029-32-1) grown by physical vapor deposition on Ag(111). As an example for the analysis of FFTs of scanning probe images we discuss the case of stacked heteroepitaxial monolayers of vanadyl phthalocyanine (VOPc, CAS No.: 13930-88-6) on PTCDA on Ag(111). Finally, we demonstrate the indexing of SAED patterns on the example of a cross section of an anatase (TiO$_2$, CAS No.: 1317-70-0) thin film, epitaxially grown on a LaAlO$_3$(100) substrate. The chemical structures of the substances used as adlayers in this work are depicted in Fig. 1.

II. METHODS

A. Fundamentals

For the following mathematical treatise, a crystal-fixed Cartesian coordinate system is assumed such that the real-space lattice vector $\mathbf{a}_0$ is aligned in the x axis and $\mathbf{b}_0$ lies in the xy plane; a, b, and γ are the parameters of the direct unit cell (rhomboid).

Then the reciprocal lattice vector $\mathbf{g}$ with its Laue indices h and k can be represented by the equation

$$\mathbf{g} = \begin{pmatrix} g_x \\ g_y \end{pmatrix} = A_0^* \begin{pmatrix} h \\ k \end{pmatrix}. \tag{1}$$

The matrix A_0^* is given as

$$A_0^* = \begin{pmatrix} \frac{2\pi}{a} & 0 \\ -\frac{2\pi \cos\gamma}{a \sin\gamma} & \frac{2\pi}{b \sin\gamma} \end{pmatrix}. \tag{2}$$

When the Laue condition is fulfilled, i.e., scattering vector $\mathbf{q} = \mathbf{g}$, diffraction can be observed.

In the real space, A_0 characterizes the matrix of the lattice vectors $\mathbf{a}_0$ and $\mathbf{b}_0$, which is in the nonrotated system given by

$$A_0 = \begin{pmatrix} \mathbf{a}_0 \\ \mathbf{b}_0 \end{pmatrix} = \begin{pmatrix} a & 0 \\ b \cos\gamma & b \sin\gamma \end{pmatrix} \tag{3}$$

The area A of the rhomboid can be calculated by

$$A = \det(A_0) = ab \sin\gamma. \tag{4}$$

Equations (2) and (3) are connected via

$$A_0 = 2\pi A_0^{*-1}. \tag{5}$$

Additionally, a rotational component in the xy plane has to be considered. Then, the reciprocal vector $\mathbf{g} = (g_x, g_y)^{\mathrm{T}}$ can be expressed as

$$\mathbf{g} = R(\varphi) A_0^* \begin{pmatrix} h \\ k \end{pmatrix}, \tag{6}$$

where $R(\varphi)$ performs a rotation in the xy plane counterclockwise by an angle φ and is explicitly written as

$$R(\varphi) = \begin{pmatrix} \cos\varphi & -\sin\varphi \\ \sin\varphi & \cos\varphi \end{pmatrix}. \tag{7}$$

From Eq. (6), using Eq. (5), it follows that

$$\begin{pmatrix} h \\ k \end{pmatrix} = A_0^{*-1} R(\varphi)^{\mathrm{T}} \mathbf{g} = A^{*-1} \mathbf{g} = \frac{1}{2\pi} A_0 R(\varphi)^{\mathrm{T}} \mathbf{g} \tag{8}$$

$A^* = (\mathbf{a}^*, \mathbf{b}^*)$ is explicitly written as

$$A^* = \begin{pmatrix} \frac{2\pi}{a \sin\gamma} \sin(\gamma + \varphi) & -\frac{2\pi}{b \sin\gamma} \sin\varphi \\ -\frac{2\pi}{a \sin\gamma} \cos(\gamma + \varphi) & \frac{2\pi}{b \sin\gamma} \cos\varphi \end{pmatrix}. \tag{9}$$

With

$$A = A_0 R(\varphi)^{\mathrm{T}}, \tag{10}$$

Eq. (6) can be equivalently expressed as

$$A\mathbf{g} = \begin{pmatrix} \mathbf{a} \\ \mathbf{b} \end{pmatrix} \mathbf{g} = 2\pi \begin{pmatrix} h \\ k \end{pmatrix}, \tag{11}$$
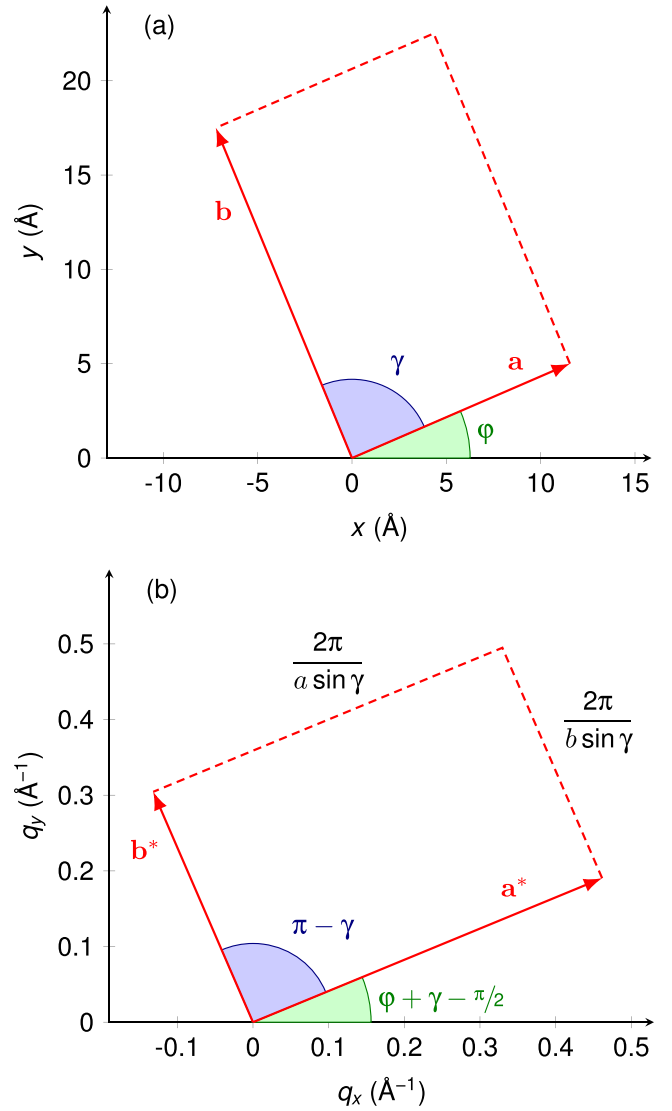

FIG. 2. Schematic two-dimensional unit cell (rhomboid) of PTCDA/Ag(111) (a) in real space and (b) in reciprocal space. The used grid represents the laboratory coordinate system.

where $\mathbf{a}$ and $\mathbf{b}$ are the rotated lattice vectors. A can be explicitly written as

$$A = \begin{pmatrix} \mathbf{a} \\ \mathbf{b} \end{pmatrix} = \begin{pmatrix} a \cos\varphi & a \sin\varphi \\ b \cos(\gamma + \varphi) & b \sin(\gamma + \varphi) \end{pmatrix} \tag{12}$$

with the relations $|\mathbf{a}| = a$, $|\mathbf{b}| = b$ and $\mathbf{a} \cdot \mathbf{b}/(ab) = \cos\gamma$. For a phase shift of 180° of either the lattice vectors $\mathbf{a}$ and $\mathbf{b}$ [i.e., $\varphi \to \varphi + \pi$ in Eq. (12)] or the reciprocal vector $\mathbf{g}$, for the Laue indices in Eq. (11) the following transformations are valid: $h \to -h$ and $k \to -k$. In Fig. 2, the unit cells are schematically shown for the real and reciprocal space, using the lattice parameters of PTCDA.

If two reciprocal vectors $\mathbf{g}_1$ and $\mathbf{g}_2$ are given, Eq. (11) can be expanded to the following relation:

$$G \begin{pmatrix} \mathbf{a} \\ \mathbf{b} \end{pmatrix}^{\mathrm{T}} = GA^{\mathrm{T}} = 2\pi H^{\mathrm{T}}, \tag{13}$$

where

$$G = \begin{pmatrix} g_{x1} & g_{y1} \\ g_{x2} & g_{y2} \end{pmatrix}, \tag{14}$$

and (h_i, k_i) are the corresponding pairs of Laue indices with

$$H = \begin{pmatrix} h_1 & h_2 \\ k_1 & k_2 \end{pmatrix}. \tag{15}$$

Equation (13) can be equivalently expressed as

$$A^{\mathrm{T}} = 2\pi G^{-1} H^{\mathrm{T}} \tag{16}$$

Furthermore, as the area $A = \det(A) = \det(A_0)$, the following relation for the determinants of G and H is valid:

$$|\det(G)| = (2\pi)^2 |\det(H)|/A. \tag{17}$$

B. Reduced unit cell (rhomboid)

If **a** and **b** are the lattice vectors of the reduced cell (rhomboid), then every linear combination **a′** and **b′** of these vectors, mathematically expressed as $A' = (\mathbf{a'}, \mathbf{b'})^{\mathrm{T}} = NA$, can be regarded as superlattice. N is the transformation matrix, which is explicitly written as

$$N = \begin{pmatrix} n_{11} & n_{12} \\ n_{21} & n_{22} \end{pmatrix}, \tag{18}$$

where n_{ij} are integers.

Considering Eqs. (8) and (6), the following relations are valid:

$$A' = NA = 2\pi NA^{*-1} = 2\pi A'^{*-1} \Leftrightarrow A^* = A^{*'} N, \quad (19)$$

$$A^* \begin{pmatrix} h \\ k \end{pmatrix} = A^{*'} N \begin{pmatrix} h \\ k \end{pmatrix} = A^{*'} \begin{pmatrix} h' \\ k' \end{pmatrix} \Rightarrow \begin{pmatrix} h' \\ k' \end{pmatrix} = N \begin{pmatrix} h \\ k \end{pmatrix}, \quad (20)$$

where h' and k' are the Laue indices in the transformed system. Thus, the transformation N that converts the lattice vectors is the same that converts the Laue indices in the reciprocal space.

The unit cell vectors must be solutions to all reciprocal vectors $\mathbf{g}_i$, which, according to Eq. (11) can be written as

$$A \mathbf{g}_i = 2\pi \mathbf{h}_i, \tag{21}$$

where $\mathbf{g}_i = (g_{xi}, g_{yi})^{\mathrm{T}}$ and $\mathbf{h}_i = (h_i, k_i)^{\mathrm{T}}$.

From Eq. (16) it can be deduced that $2\pi G^{-1}\mathbf{m}$, the product of the inverse matrix of two reciprocal vectors with a vector **m**, consisting of a doublet of arbitrary integers (m_1, m_2), leads to a vector of the reduced cell, if **m** matches $(h_1, h_2)^{\mathrm{T}}$ or $(k_1, k_2)^{\mathrm{T}}$. If a transformation matrix N exists so that **m** equals $N(h_1, h_2)^{\mathrm{T}}$ or $N(k_1, k_2)^{\mathrm{T}}$, a vector of a superlattice is obtained. According to Eq. (17), it is favorable to select two reciprocal vectors whose matrix results in a determinant which equals ± 1. Otherwise, Eq. (21) may not be valid for all reciprocal vectors. The reduced rhomboid is obtained by choosing the two shortest vectors which are not collinear and whose scalar products with all reciprocal vectors yield integers. This reduced rhomboid is equivalent to the Buerger cell in the three-dimensional case [44]. Analogously, the Niggli criteria [45] can be adapted to the two-dimensional case:

$$a \leqslant b \quad \text{and} \quad b|\cos\gamma| \leqslant \frac{a}{2}. \tag{22}$$

C. Indexing

We suggest the following procedure for indexing an unknown 2D crystalline system represented by a discrete set of reflections:

(1) Pairs of reciprocal vectors in all possible combinations are formed, i.e., if n vectors are given, these are $\frac{n!}{(n-2)!2!} = \frac{n(n-1)}{2}$ pairs $(\mathbf{g}_1, \mathbf{g}_2)$, where $\mathbf{g}_1$ and $\mathbf{g}_2$ are any two reciprocal vectors. According to Eq. (17), if the pair corresponds to a unit rhomboid, the determinant of its matrix is indirectly proportional to the area of this rhomboid, if the determinant of the matrix of the corresponding Laue indices equals ± 1. According to Eq. (14), the selected pairs of reciprocal vectors are combined to matrices. If they belong to the same system, their inverse matrices multiplied with the vectors of the corresponding Laue indices will result in the vectors of the rhomboid [cf. Eq. (16)]. This can be achieved by multiplying the inverse matrices G^{-1} with vectors $2\pi(m_1, m_2)^{\mathrm{T}}$, where the integers m_i are systematically varied in a reasonable range of Laue indices (e.g., between -5 and 5). Then, lattice vectors of the rhomboid and of its superlattices are obtained. The vectors are sorted according to their lengths, and in ascending order, two vectors, which are not collinear, are selected. Chosen boundary conditions, e.g., for the expected vector lengths, and the inequalities (22) restrict the possible solutions.

(2) The tentative cell matrices are multiplied with all reciprocal vectors. If the scalar products yield integers [i.e., the corresponding Laue indices according to Eq. (21)], the matrices and reciprocal vectors belong to the same system. Due to experimental uncertainties, error intervals must be considered. For a system of reciprocal vectors, the rhomboid with the smallest deviations from integers will be chosen. Solutions with a larger number of associated reciprocal vectors will be preferred.

(3) From the cell matrix, the cell parameters a, b, and γ as well as the angle φ can be obtained [cf. Eq. (12)]. According to Eq. (16), the unit cell vectors can be calculated from every linearly independent pair of reciprocal lattice vectors of the same system. This redundancy can be used to determine mean values and standard deviations of the unit cell parameters. Furthermore, the matrix of the unit cell vectors can be optimized using various procedures (see the Supplemental Material).

In passing we note that the only required input from a measurement is the pattern of the reciprocal lattice (i.e., the spot positions with the coordinates q_x and q_y in units of Å^{-1}), independent of the way those data were obtained (except for the calibration and experimental resolution, of course). However, a useful strategy to greatly increase the precision is to exploit the *a priori* known properties, if any, of the system (e.g., minimum and/or maximum values for the lattice constants and the area of the unit cell).

D. Multiple scattering

In indexing LEED data, a special challenge arises due to multiple scattering [30,46] which occurs much less frequently in GIXD [47]. This can be rationalized by the much lower scattering cross section of x rays as compared to electrons [48]. If the reciprocal vector **g** has components of both the

adsorbate and the substrate, it can be written as follows:

$$\mathbf{g} = \mathbf{a}_a^* h_a + \mathbf{b}_a^* k_a + \mathbf{a}_s^* h_s + \mathbf{b}_s^* k_s, \tag{23}$$

where $\mathbf{a}_a^*$, $\mathbf{b}_a^*$ and $\mathbf{a}_s^*$, $\mathbf{b}_s^*$ are the reciprocal lattice vectors and h_a, k_a and h_s, k_s are the Laue indices of the adsorbate and the substrate, respectively. As the reciprocal lattice vectors of the substrate can be determined independently, in a "first guess" the reciprocal vectors of the adsorbate are determined assuming scattering of zeroth order, i.e., $h_s = k_s = 0$. Then, the Laue indices are chosen so that the residual error for each measured reciprocal vector $\mathbf{q}$ is as small as possible. As Eq. (23) can be expressed as

$$\mathbf{a}_a^* h_a + \mathbf{b}_a^* k_a = \mathbf{g}' = \mathbf{g} - \mathbf{a}_s^* h_s - \mathbf{b}_s^* k_s, \tag{24}$$

$\mathbf{a}_a^*$ and $\mathbf{b}_a^*$ can be optimized as in the previous case. At room temperature, the lattice parameters for Ag(111) are $a_s = b_s = 2.888\,\text{Å}$ and $\gamma_s = 120°$ (sometimes, $60°$ is used instead). The angle φ_s must be determined experimentally, using diffraction reflections of the substrate.

The reciprocal vectors of the adsorbate and substrate can linearly combine so that in real space they give rise to super cells. Our indexing algorithm may find such super cells, but they usually possess only few numbers of associated reciprocal lattice vectors in comparison with the reduced cell of the adsorbate. In periodic overlayers on hexagonal metal substrates, as in the case of Ag(111), these super cells result in periodic Moiré patterns when imaged in real space, and in satellite spots around the adsorbate lattice spots in LEED or in the respective FFT of the real space image.

E. Epitaxy matrix

In organic systems, the epitaxial growth of molecular overlayers depends on a delicate balance of weak noncovalent interactions between the molecules in the overlayer and interactions of various kinds between the molecules and the substrate, with strongly varying strengths. For inorganic adsorbates, the same holds true, albeit with covalent adsorbate-adsorbate interactions being involved typically to a greater extent. Usually, the limiting cases of physisorption and chemisorption are distinguished [49–52]. The large size and typical low symmetry of the unit cells often prohibit commensurism where each molecule of the overlayer resides on symmetry equivalent substrate lattice sites. However, other degrees of registry are well known to occur frequently, especially on-line coincidences. For a recent review and classification, see Ref. [27]. A 2D matrix can be used that describes the epitaxial interface. For the epitaxy matrix $\mathbf{M}$,

$$\mathbf{M} = \begin{pmatrix} M_{11} & M_{12} \\ M_{21} & M_{22} \end{pmatrix}, \tag{25}$$

the following relation is valid:

$$\begin{pmatrix} \mathbf{a}_a \\ \mathbf{b}_a \end{pmatrix} = \mathbf{A}_a = \mathbf{M}\mathbf{A}_s = \mathbf{M} \begin{pmatrix} \mathbf{a}_s \\ \mathbf{b}_s \end{pmatrix}, \tag{26}$$

where $\mathbf{a}_a$ and $\mathbf{b}_a$ are the lattice vectors of the adsorbate (molecular overlayer), and $\mathbf{a}_s$ and $\mathbf{b}_s$ are the lattice vectors of the substrate, and $\mathbf{A}_a$ and $\mathbf{A}_s$ the associated matrices [cf. Eq. (12)].

As $\mathbf{A}_s^{-1} = \frac{1}{2\pi} \mathbf{A}_s^*$, from Eq. (26), the following relation can be deduced:

$$\mathbf{M} = \frac{1}{2\pi} \mathbf{A}_a \mathbf{A}_s^*. \tag{27}$$

Using Eqs. (9) and (12), this can be explicitly written as

$$\mathbf{M} = \begin{pmatrix} \frac{a_a}{a_s \sin \gamma_s} \sin (\gamma_s - \Delta\varphi) & \frac{a_a}{b_s \sin \gamma_s} \sin \Delta\varphi \\ \frac{b_a}{a_s \sin \gamma_s} \sin (\gamma_s - \gamma_a - \Delta\varphi) & \frac{b_a}{b_s \sin \gamma_s} \sin (\gamma_a + \Delta\varphi) \end{pmatrix} \tag{28}$$

with $\Delta\varphi = \varphi_a - \varphi_s$. Then, for the determinant $\det(\mathbf{M})$ the following expression is valid:

$$\det(\mathbf{M}) = \frac{a_a b_a \sin \gamma_a}{a_s b_s \sin \gamma_s}. \tag{29}$$

From Eq. (28) the following relations can be derived:

$$\cot \Delta\varphi = \cot \gamma_s + \frac{M_{11}}{M_{12}} \frac{a_s}{b_s \sin \gamma_s}, \tag{30}$$

$$\cot (\gamma_a + \Delta\varphi) = \cot \gamma_s + \frac{M_{21}}{M_{22}} \frac{a_s}{b_s \sin \gamma_s}, \tag{31}$$

$$a_a = M_{12} \frac{b_s \sin \gamma_s}{\sin \Delta\varphi}, \tag{32}$$

and

$$b_a = M_{22} \frac{b_s \sin \gamma_s}{\sin (\gamma_a + \Delta\varphi)}. \tag{33}$$

If $M_{21} = 0$, it follows that $\Delta\varphi = 0$ and $a_a = M_{11} a_s \sin \gamma_s$. Hence, knowing the elements of the epitaxy matrix and the lattice parameters of the substrate, allows calculating the lattice parameters of the adsorbate and the azimuthal angle $\Delta\varphi$.

In the case of commensurism ("point-on-point" epitaxy), all elements of the matrix are integers. Therefore, each lattice vector of the adsorbate is a linear combination of the substrate lattice vectors with integer coefficients. Higher order commensurism (HOC) is similar, yet at least one element of the matrix is a (noninteger) rational number, while an adsorbate supercell (i.e., a reasonably small number of connected primitive adsorbate unit cells) can be found whose epitaxy matrix consists of integers only. Commensurism and HOC both imply that the substrate lattice and the adsorbate lattice have two linearly independent common periodicities. Aside from those, the so-called on-line coincidences (OLC) are characterized by a match of adsorbate and substrate lattices in just one direction [27]. This can be best visualized by the method of projecting the adsorbate lattice points onto one substrate unit cell [27,53]. On the one hand, the projection patterns of commensurate and HOC registries are discrete sets of equidistant points. For OLC registries, on the other hand, the projected adsorbate lattice points run along equidistant lines, hence the name "on-line coincident". In all these cases, only specific parts of the substrate unit cell are accessible by adsorbate lattice points, which gives rise to the avoidance of energetically unfavorable adsorption sites. It can be shown mathematically that even epitaxy matrices consisting of four irrational elements can satisfy, under well-defined circumstances, the conditions of an on-line coincidence [27]. Therefore, it is not always obvious to either recognize or rule out an OLC registry merely based on the appearance of the epitaxy matrix elements.

TABLE I. Parameters used for the deposition of the molecular films, including the temperatures of the substrate and effusion cell during deposition, the deposition time and whether an additional annealing step was performed.

Molecule	$T_{\text{substrate}}$ (K)	T_{source} (K)	$t_{\text{deposition}}$ (min)	annealing
		PTCDA/Ag(111)		
PTCDA	296	630	8	yes
		P2O/Ag(111)		
P2O	300	450	10	no
		VOPc/PTCDA/Ag(111)		
PTCDA	296	630	8	yes
VOPc	≈ 80	610	10	yes

III. EXPERIMENTAL DETAILS

Depositions of organic films were carried out in ultra-high vacuum environments with a base pressure lower than 5×10^{-10} mbar. The silver single crystal (MaTecK GmbH) was prepared by repeated cycles of Ar^+ sputtering at 700 eV with incident angles of $\pm 45°$ relative to the surface normal and subsequent annealing at 770 K. A sufficient surface quality was confirmed by means of LEED before deposition of the molecular films. P2O (Sigma Aldrich), PTCDA (Sigma Aldrich), and VOPc (Aldrich) were purchased and purified by temperature-gradient vacuum sublimation using a DSU-05 (CreaPhys GmbH) prior to use. Layer deposition was done from shutter-controlled effusion cells held at a constant temperature with the samples either kept at room temperature or cooled by liquid nitrogen in the case of the VOPc deposition (see Table I). The film growth was monitored *in situ* using differential reflectance spectroscopy (DRS) [54,55], stopping the deposition process as soon as a clear monolayer signal became apparent. The P2O monolayer on Ag(111) was used as deposited, i.e., additional annealing as in earlier experiments [15] was not performed here. For the PTCDA samples, excess molecules above one monolayer were removed by careful annealing of the sample until only the most strongly bound first molecular layer remained on the surface as indicated by

DRS. The VOPc film was gently annealed after warming to room temperature while being monitored with LEED until a well-ordered structure emerged.

LEED experiments were carried out using a dual microchannel-plate LEED (OCI Vacuum Microengineering, Inc.), all images were calibrated and corrected for distortions using LEEDCal [33,56]. Spot positions in reciprocal space were extracted using LEEDLab [57].

For STM measurements a JT-STM/AFM (SPECS Surface Nano Analysis GmbH) was used equipped with an Ar^+ sputtered tungsten tip and operated at 4.5 K.

An STM scan showing both the substrate (PTCDA, which itself was predeposited on Ag(111)) and the adsorbate (VOPc) was chosen. Further, two equally sized close-up views showing either the substrate or the adsorbate structure were cut out and Fourier transformed. The close-up view containing only the PTCDA structure and the respective FFT were analyzed for apparent lattice vectors, which still contain systematic errors due the inherent and unavoidable distortions of the STM image (e.g., shearing, stretching, compression). Upon comparing those apparent lattice vectors to the lattice vectors expected for the PTCDA monolayer on Ag(111), which are known from the literature [17] and used in this work as a benchmark for our indexing algorithm (cf. LEED data in the Supplemental Material), we obtain a correction matrix that is able to compensate distortions and linear calibration errors typically present in scanning probe microscopy measurements. By assuming the distortions to be describable by a linear transformation over the whole scan, the same correction matrix can then be applied to other parts of the scan, effectively using the substrate (here PTCDA) as a reference structure for the calibration and for the determination of an unknown adsorbate structure (here VOPc).

Reciprocal lattice vectors for the VOPc structure were then determined from the features apparent in the respective FFT by using LEEDLab, with the extracted centers of the FFT features adjusted to the appropriate positions by use of the above correction matrix.

The anatase films were grown on $LaAlO_3(100)$ substrates by means of pulsed laser deposition at the APE beam line

TABLE II. Unit cell parameters a, b, γ for and resulting area of PTCDA/Ag(111) and P2O/Ag(111), experimentally obtained from LEED experiments. The orientations of the a axis of the molecular lattices are specified by the angles $\Delta\varphi$ indicating rotation with respect to the [1 $\bar{1}$ 0] axis of Ag(111). Mean values and standard deviations of all parameter sets are calculated over all azimuthal orientations of each unit cell. Additionally, the epitaxy matrices and their determinants are itemized. The expected values, if the elements of the epitaxy matrices are rounded to the indicated values, are given in italics. Note that the lattice parameters for an as-deposited P2O monolayer, given here, differ in fact from an annealed P2O monolayer [15] and from a comparatively thick P2O film on Ag(111) [26].

a (Å)	b (Å)	γ (°)	Area (Å^2)	$\Delta\varphi$ (°)	Epitaxy matrix $\boldsymbol{M}$	det($\boldsymbol{M}$)
			PTCDA/Ag(111)			
12.5879(15)	18.9364(12)	89.001(14)	238.32(2)	23.412(5)	$\begin{pmatrix} 4.9999 & 2.0000 \\ 0.9999 & 6.9990 \end{pmatrix}$	32.995
12.5885	*18.9379*	*88.998*	*238.36*	*23.413*	$\begin{pmatrix} 5 & 2 \\ 1 & 7 \end{pmatrix}$	*33.000*
			P2O/Ag(111)			
8.1683(48)	14.060(28)	92.446(77)	114.74(24)	6.670(80)	$\begin{pmatrix} 3.0000 & 0.3813 \\ 1.9998 & 5.5512 \end{pmatrix}$	15.891
8.1693	*14.0635*	*92.461*	*114.78*	*6.704*	$\begin{pmatrix} 3 & 0.3813 \\ 2 & 5.5512 \end{pmatrix}$	*15.891*

of IOM-CNR at the synchrotron Elettra in Trieste [58]. For details on this sample the reader is referred to preceding work [59,60]. Cross-sectional TEM samples were then prepared with a conventional polishing technique followed by dimpling and ion milling [60]. For SAED a JEOL 2010 UHR TEM was used, equipped with a field emission gun and operated at 200 kV. The data was acquired with a Gatan CCD camera with a resolution of 1024 × 1024 pixel using the Gatan Microscopy Suite (GMS, v. 1.4). Spot positions of the SAED pattern were extracted using LEEDLab [57], scaling was carried out using a correction matrix determined from the reflexes associated with $LaAlO_3$ with the unit cell size taken from the literature [61,62].

IV. RESULTS AND DISCUSSION

Regarding the following selection of experimental data, we emphasize that the chemical nature of the samples is not of particular importance for this work, which is instead focused on 2D reciprocal lattices and the analysis thereof. By using various kinds of adsorbate/substrate systems we underline the universality of our method and deliberately do not restrict ourselves to either organic or inorganic adlayers. Moreover, our indexing algorithm can be equally applied to all kinds of 2D patterns in reciprocal space where a crystallographic indexing is required, e.g., electron diffraction data (such as LEED, TED/SAED) and FFTs of scanning probe images. Having thoroughly tested our method on the well-known benchmark example of PTCDA on Ag(111) (see the Supplemental Material [63]), we will now discuss several other examples covering different application areas of our indexing algorithm.

A. P2O on Ag(111)

In this work, an as-deposited P2O monolayer on Ag(111) is examined, which differs structurally from an annealed P2O monolayer [15] and from a comparatively thick P2O film on Ag(111) [26]. Noticeably, Wang *et al.* reported LEED and STM measurements of P2O on Ag(111), but they did not elaborate on the epitaxial alignment between adsorbate and substrate lattices by analyzing their data in reciprocal space [70]. Judging from the P2O lattice parameters provided in their paper ($a = 8.1$ Å, $b = 15.9$ Å, $\gamma = 86°$) we suppose that their structure differs from the one we discuss in the following.

Based on our LEED experiment, 70 reciprocal lattice vectors could be obtained. The indexing procedure on these data resulted in 12 solutions with individual lattice vectors **a** and **b**, and two groups of azimuthal alignments, each with a 60°-symmetry. About 85% of the observed diffraction points could be explained by the reciprocal lattice vectors of the adsorbate. By considering multiple scattering and including the reciprocal lattice vectors of Ag(111), all diffraction points could be assigned, and the resulting lattice parameters were refined (see Table II). The data demonstrate a point-on-line epitaxial relationship [27] between monolayer and substrate. In Fig. 3, the (q_x, q_y) positions of the extracted diffraction peaks and the corresponding calculated values from the indexing result are shown, itemized for multiple scattering of zeroth and higher order and the different azimuthal alignments.
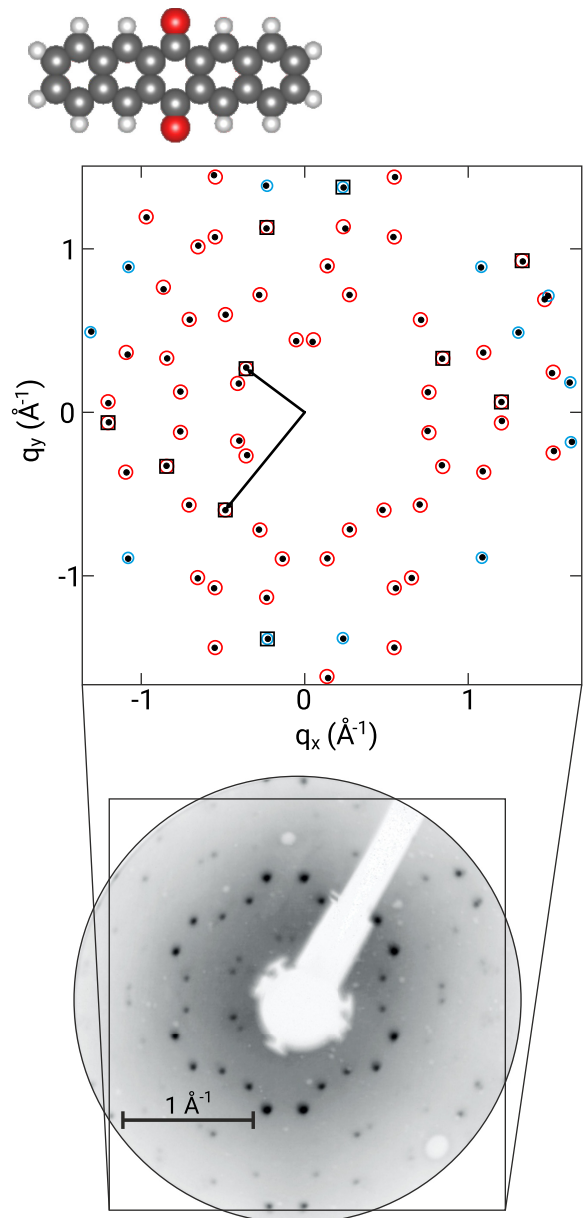

FIG. 3. Positions of experimentally determined diffraction peaks of a P2O monolayer grown on Ag(111), obtained from a LEED experiment at 35.5 eV (image contrast inverted and enhanced). Given are the (q_x, q_y) positions of the discernible diffraction peaks (black dots). Results of the indexing of epitaxially grown oriented crystals are also shown. Multiple scattering in the LEED experiment is differentiated by contributions of zeroth (red circles) and higher order (small blue circles). The extracted reciprocal unit cell vectors and the corresponding spots are highlighted for one orientation only (black arrows and open squares).

B. VOPc on PTCDA on Ag(111)

The lattice parameters of the substrate (here consisting of a PTCDA monolayer that was predeposited on a Ag(111) surface) are known from the literature [17,69] and summarized in Table II. The STM image in Fig. 4 shows this PTCDA structure in the upper left corner. As explained in the Experimental Details, this part of the STM scan was used to determine the
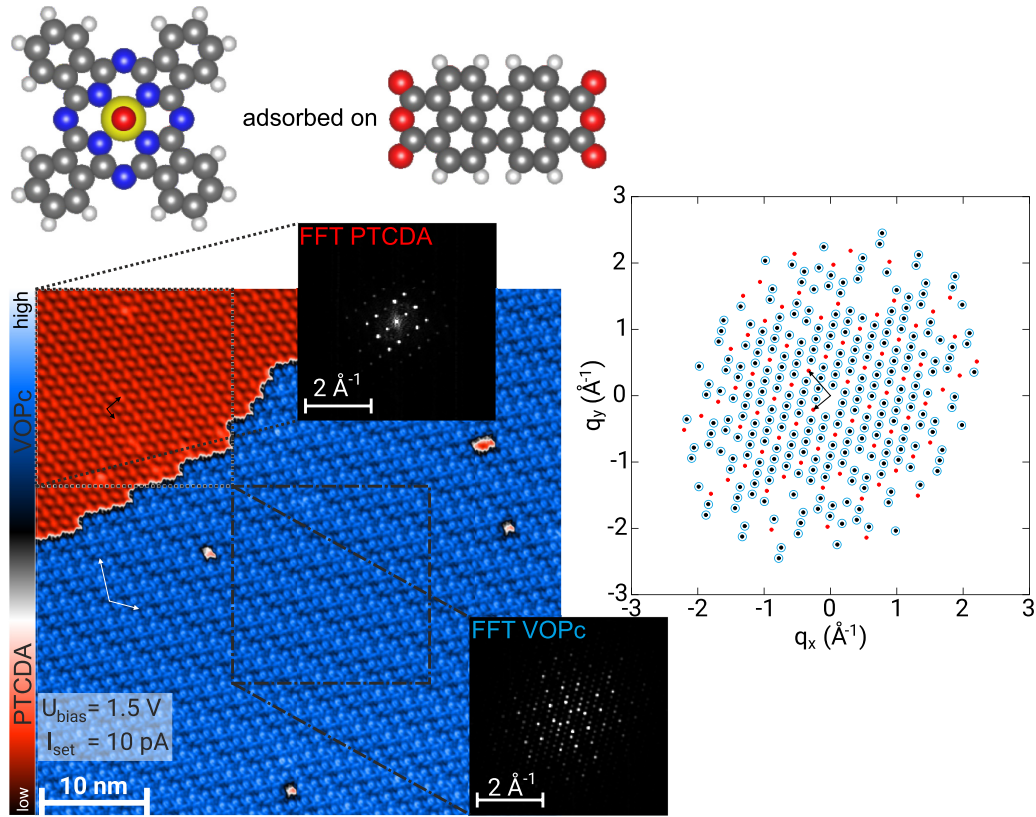
FIG. 4. Positions of experimentally determined reciprocal space spot positions of VOPc grown on PTCDA/Ag(111) obtained from an STM experiment via FFT. Given are the (q_x, q_y) positions of the discernible FFT features (black dots). Results of the indexing are marked by circles. The Moiré contrast in the STM image is differentiated by contributions of the substrate (PTCDA, red circles) and additional spots by the adsorbate (VOPc, blue circles). Extracted real-space unit cell vectors are superimposed on the STM image for PTCDA (black) and the large VOPc unit cell (white). The reciprocal lattice vectors of PTCDA are shown in the right panel (black arrows).

distortions – inevitably present in scanning probe microscopy – by comparing the corresponding FFT to the LEED results. In this manner, we calibrated the STM image by making use of a known reference structure (i.e., PTCDA), and this distortion correction was applied to the unknown adsorbate structure (i.e., VOPc) in the same STM image.

TABLE III. Unit cell parameters a, b, γ for and resulting area of VOPc/PTCDA (large and small unit cell) and anatase/LaAlO$_3$. The orientations of the a axis of the molecular lattices are specified by the angles $\Delta\varphi$ indicating rotation with respect to the main axis of the substrate. Additionally, the epitaxy matrices and their determinants are itemized. The expected values, if the elements of the epitaxy matrices are rounded to the indicated values, are given in italics.

a (Å)	b (Å)	γ (°)	Area (Å^2)	$\Delta\varphi$ (°)	Epitaxy matrix $\boldsymbol{M}$	det($\boldsymbol{M}$)
		VOPc/PTCDA (comprising 6 VOPc molecules)				
31.021(45)	40.122(50)	107.57(8)	1187	−37.11(6)	$\begin{pmatrix} 1.9910 & -0.9884 \\ 1.0137 & 1.9965 \end{pmatrix}$	4.977
31.241	*40.128*	*108.03*	*1192*	*−37.31*	$\begin{pmatrix} 2 & -1 \\ 1 & 2 \end{pmatrix}$	*5.000*
		VOPc/PTCDA (comprising 1 VOPc molecule)				
13.940(63)	14.209(67)	90.88(26)	198.0	−64.33(19)	$\begin{pmatrix} 0.4971 & -0.6634 \\ 1.0009 & 0.3354 \end{pmatrix}$	0.831
14.011	*14.181*	*90.74*	*198.7*	*−64.31*	$\begin{pmatrix} 0.5 & -0.6666 \\ 1 & 0.3333 \end{pmatrix}$	*0.833*
		Anatase/LaAlO$_3$(100) (in cross section)				
3.792(11)	9.454(25)[a]	90.01(10)		0.011(10)	Not applicable	
		LaAlO$_3$(100) (in cross section)				
3.787(11)	3.787(11)	90.00(8)			Not applicable	

[a]Note that b is oriented perpendicular to the interface between anatase and LaAlO$_3$(100), and thus neither an epitaxy matrix nor an area of the surface unit cell can be assigned in this case.

For the VOPc adlayer, highlighted in blue in Fig. 4, 336 reciprocal lattice vectors were obtained. Searching for the smallest VOPc cell which can explain all diffraction spots, we found the following parameters: $a = 31.0221$ Å, $b = 40.1221$ Å, and $\gamma = 107.573°$. The data demonstrate a commensurate epitaxial relation between the VOPc mono-layer and the PTCDA substrate (see Table III). This unit cell comprises 6 VOPc molecules and is capable of explaining the FFT features as well as the contrast observed in the STM image. However, the same FFT pattern could also be produced in theory by a unit cell with a lower number of molecules, if the structure were to exhibit a Moiré contrast. Thus, searching for a smaller unit cell, the following solution could be found as well: $a = 13.9408$ Å, $b = 14.2091$ Å, and $\gamma = 90.878°$ (see Table III). By comparing the area of both solutions, the smaller unit cell contains one VOPc molecule instead of six. 91 diffraction peaks can be explained by the adsorbate, the others by multiple scattering up to the third order (see Fig. 4).

Whether the structure is a real supercell with symmetry inequivalent orientations and/or positions of the six VOPc molecules within the unit cell or whether the observed contrast is an effect of the superposition of the two involved lattices, i.e., a Moiré pattern stemming from the superposition of the PTCDA and VOPc lattices, cannot be deduced solely from the measurement of the latter. For the comparable system of copper-II-phthalocyanine (CuPc, CAS No.: 147-14-8) on PTCDA on Ag(111) a similar contrast modulation was found by others and interpreted as the result of a supercell containing 6 CuPc molecules [71]. Given the similarity of both systems we consider this to be the most plausible explanation for VOPc as well.

C. Anatase on LaAlO₃(100)

Finally, we demonstrate the capability of our algorithm to analyze the epitaxy of an anatase (tetragonal) thin film grown on a LaAlO₃(100) substrate (pseudocubic), from an SAED pattern that was acquired in cross section. From the present pattern in Fig. 5, 35 reciprocal vectors were obtained. Two unit cells with different parameters could be identified. Partially overlapping, 27 diffraction peaks could be assigned to anatase, and 17 diffraction spots were assigned to the substrate. In Fig. 5, also the (q_x, q_y) positions of the extracted diffraction peaks and the corresponding calculated values from the indexing procedure for anatase and LaAlO₃ are shown. The obtained lattice parameters are listed in Table III. The out-of-plane parameter b of the film is aligned with the anatase [001] crystallographic orientation and was measured here to be 9.454 Å, in good agreement with the corresponding parameter of the anatase unit cell, which is due to the very low lattice mismatch between substrate and film (0.1%) [72]. This low mismatch is further confirmed by the value for the in-plane parameter a of the film, which has been found to be very close to the value for LaAlO₃ of 3.787 Å [62]. The excellent match between the two crystals in their present orientation is also reflected in the measured value for γ of almost exactly 90°.
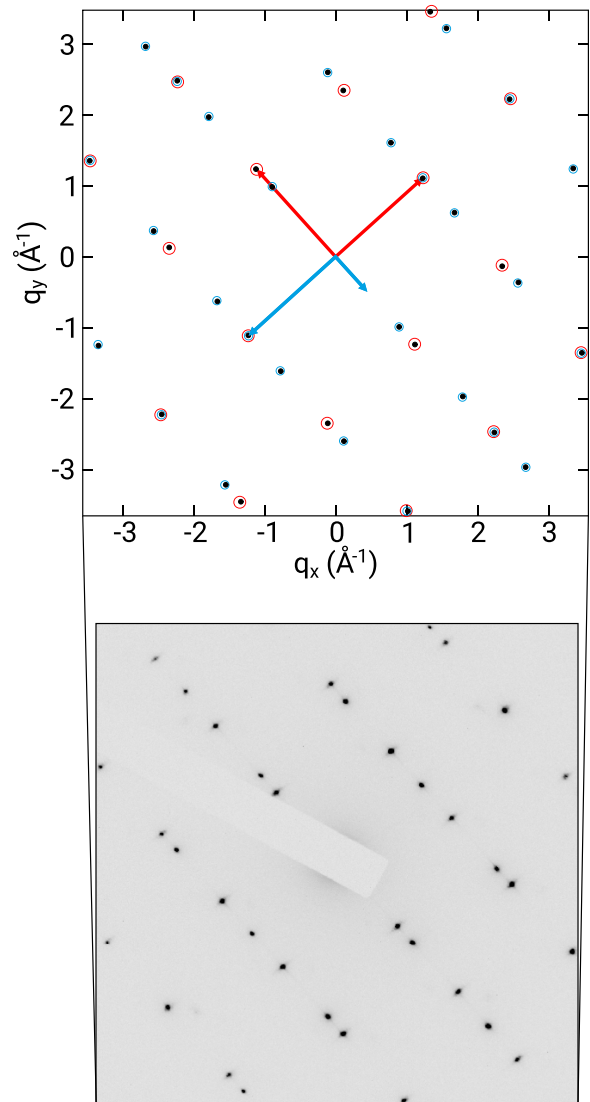

FIG. 5. Positions of experimentally determined diffraction peaks of the anatase thin film grown on LaAlO₃(100) obtained from an SAED experiment acquired in cross section (contrast inverted). Given are the (q_x, q_y) positions of the discernible diffraction peaks (black dots). The results of the indexing of LaAlO₃ and anatase crystals are shown as red circles and small blue circles, respectively. Each reciprocal lattice is represented by an independent set of vectors drawn in red for LaAlO₃ and blue for anatase.

V. CONCLUSION

In this work, we present an algorithm for indexing 2D patterns in reciprocal space, which can be applied to all kinds of experimental results where 2D reciprocal lattice vectors are obtained. It is noteworthy that the algorithm is not limited to experimental diffraction methods but can also be used for the analysis of FFTs, achieved mathematically from real space STM or AFM images with sufficient atomic or molecular resolution.

We demonstrate the successful applicability for various kinds of organic and inorganic adlayers for which the 2D

reciprocal patterns were obtained by LEED, TED/SAED, or FFT of respective STM images. In all those cases the 2D reciprocal spot patterns could be fully explained and indexed including even multiple scattering where necessary. From the automatic indexing, the real space lattice parameters of all adsorbates are obtained. In both LEED investigations, 12 unit cells with the same lattice constants but different orientations were identified. In the case of TED/SAED, two different unit cells (LaAlO$_3$ and anatase) could be assigned. Further, based on a recent classification of epitaxy types [27], the specific epitaxy types are identified, ranging from commensurate to on-line coincident.

Our algorithm provides mathematical solutions to the imposed algebraic equation system, seeking for unit cells that obey the crystallographic conventions and can explain all reflexes lying within an *a priori* user defined tolerance, and optimized to minimize the residual errors. Complex systems comprising unit cells with different orientations or parameters can be analyzed. It should be stressed, however, that in certain cases, the definite solution must be selected from various possible ones by imposing experimentally found boundary conditions on the cell parameters.

[1] R. Taylor and P. A. Wood, Chem. Rev. **119**, 9427 (2019).

[2] A. O. F. Jones, B. Chattopadhyay, Y. H. Geerts, and R. Resel, Adv. Funct. Mater. **26**, 2233 (2016).

[3] Y. Diao, K. M. Lenn, W.-Y. Lee, M. A. Blood-Forsythe, J. Xu, Y. Mao, Y. Kim, J. A. Reinspach, S. Park, A. Aspuru-Guzik *et al.*, J. Am. Chem. Soc. **136**, 17046 (2014).

[4] C. Schuenemann, A. Petrich, R. Schulze, D. Wynands, J. Meiss, M. P. Hein, J. Jankowski, C. Elschner, J. Alex, M. Hummert *et al.*, Org. Electron. **14**, 1704 (2013).

[5] B. Reisz, V. Belova, G. Duva, C. Zeiser, M. Hodas, J. Hagara, P. Šiffalovič, L. Pithan, T. Hosokai, A. Hinderhofer *et al.*, J. Appl. Cryst. **54**, 203 (2021).

[6] L. Jiao, H. J. Liu, J. L. Chen, Y. Yi, W. G. Chen, Y. Cai, J. N. Wang, X. Q. Dai, N. Wang, W. K. Ho *et al.*, New J. Phys. **17**, 053023 (2015).

[7] B. Munkhbat, A. B. Yankovich, D. G. Baranov, R. Verre, E. Olsson, and T. O. Shegai, Nat. Commun. **11**, 4604 (2020).

[8] H. Tian, J.-Q. Zhang, W. Ho, J.-P. Xu, B. Xia, Y. Xia, J. Fan, H. Xu, M. Xie, and S. Y. Tong, Matter **2**, 111 (2020).

[9] D. Nazzari, J. Genser, V. Ritter, O. Bethge, E. Bertagnolli, G. Ramer, B. Lendl, K. Watanabe, T. Taniguchi, R. Rurali *et al.*, J. Phys. Chem. C **125**, 9973 (2021).

[10] S. H. Choi, H.-J. Kim, B. Song, Y. I. Kim, G. Han, H. T. T. Nguyen, H. Ko, S. Boandoh, J. H. Choi, C. S. Oh *et al.*, Adv. Mater. **33**, 2006601 (2021).

[11] C. Stadler, S. Hansen, I. Kröger, C. Kumpf, and E. Umbach, Nat. Phys. **5**, 153 (2009).

[12] D. Kasemann, C. Wagner, R. Forker, T. Dienel, K. Müllen, and T. Fritz, Langmuir **25**, 12569 (2009).

[13] P. Beyer, T. Breuer, S. Ndiaye, A. Zykov, A. Viertel, M. Gensler, J. P. Rabe, S. Hecht, G. Witte, and S. Kowarik, ACS Appl. Mater. Interfaces **6**, 21484 (2014).

[14] M. Meissner, F. Sojka, L. Matthes, F. Bechstedt, X. Feng, K. Müllen, S. C. B. Mannsfeld, R. Forker, and T. Fritz, ACS Nano **10**, 6474 (2016).

[15] A. Jeindl, J. Domke, L. Hörmann, F. Sojka, R. Forker, T. Fritz, and O. T. Hofmann, ACS Nano **15**, 6723 (2021).

[16] J. Simbrunner, B. Schrode, S. Hofer, J. Domke, T. Fritz, R. Forker, and R. Resel, J. Phys. Chem. C **125**, 618 (2021).

[17] K. Glöckler, C. Seidel, A. Soukopp, M. Sokolowski, E. Umbach, M. Böhringer, R. Berndt, and W.-D. Schneider, Surf. Sci. **405**, 1 (1998).

[18] L. Kilian, E. Umbach, and M. Sokolowski, Surf. Sci. **600**, 2633 (2006).

[19] R. Forker, J. Peuker, M. Meissner, F. Sojka, T. Ueba, T. Yamada, H. S. Kato, T. Munakata, and T. Fritz, Langmuir **30**, 14163 (2014).

[20] F. Sojka, M. Meissner, T. Yamada, T. Munakata, R. Forker, and T. Fritz, J. Phys. Chem. C **120**, 22972 (2016).

[21] M. G. Rossmann and C. G. van Beek, Acta Crystallogr. D **55**, 1631 (1999).

[22] W. Kabsch, Acta Crystallogr. D **70**, 2204 (2014).

[23] A. Morawiec, J. Appl. Cryst. **50**, 647 (2017).

[24] G. Winter, D. G. Waterman, J. M. Parkhurst, A. S. Brewster, R. J. Gildea, M. Gerstel, L. Fuentes-Montero, M. Vollmar, T. Michels-Clark, I. D. Young *et al.*, Acta Crystallogr. D **74**, 85 (2018).

[25] Y. Gevorkov, O. Yefanov, A. Barty, T. A. White, V. Mariani, W. Brehm, A. Tolstikova, R.-R. Grigat, and H. N. Chapman, Acta Crystallogr. A **75**, 694 (2019).

[26] J. Simbrunner, B. Schrode, J. Domke, T. Fritz, I. Salzmann, and R. Resel, Acta Crystallogr. A **76**, 345 (2020).

[27] R. Forker, M. Meissner, and T. Fritz, Soft Matter **13**, 1748 (2017).

[28] M. P. Seah and W. A. Dench, Surf. Interface Anal. **1**, 2 (1979).

[29] T. Graber, F. Forster, A. Schöll, and F. Reinert, Surf. Sci. **605**, 878 (2011).

[30] M. A. Van Hove, W. H. Weinberg, and C.-M. Chan, *Low-Energy Electron Diffraction: Experiment, Theory and Surface Structure Determination: Springer Series in Surface Sciences* (Springer, Berlin-Heidelberg, 1986).

[31] E. A. Soares, C. M. C. de Castilho, and V. E. de Carvalho, J. Phys.: Condens. Matter **23**, 303001 (2011).

[32] H. I. Li, K. Pussi, K. J. Hanna, L.-L. Wang, D. D. Johnson, H.-P. Cheng, H. Shin, S. Curtarolo, W. Moritz, J. A. Smerdon, R. McGrath, and R. D. Diehl, Phys. Rev. Lett. **103**, 056101 (2009).

[33] F. Sojka, M. Meissner, C. Zwick, R. Forker, and T. Fritz, Rev. Sci. Instrum. **84**, 015111 (2013).

[34] F. Sojka, M. Meissner, C. Zwick, R. Forker, M. Vyshnepolsky, C. Klein, M. Horn-von Hoegen, and T. Fritz, Ultramicroscopy **133**, 35 (2013).

[35] P. Jelínek, J. Phys.: Condens. Matter **29**, 343002 (2017).

[36] H. Mönig, Chem. Commun. **54**, 9874 (2018).

[37] L. Gross, B. Schuler, N. Pavlíček, S. Fatayer, Z. Majzik, N. Moll, D. Peña, and G. Meyer, Angew. Chem. Int. Ed. **57**, 3888 (2018).

[38] F. Joucken, F. Frising, and R. Sporken, Carbon **83**, 48 (2015).

[39] T. Kirchhuebel, M. Gruenewald, F. Sojka, S. Kera, F. Bussolotti, T. Ueba, N. Ueno, G. Rouillé, R. Forker, and T. Fritz, Langmuir **32**, 1981 (2016).

[40] A. Mehler, T. Kirchhuebel, N. Néel, F. Sojka, R. Forker, T. Fritz, and J. Kröger, Langmuir **33**, 6978 (2017).

[41] C. Zwick, M. Meissner, F. Sojka, R. Forker, and T. Fritz, Phys. Rev. Mater. **3**, 085604 (2019).

[42] D. L. Dorset, W. F. Tivol, and J. N. Turner, Ultramicroscopy **38**, 41 (1991).

[43] D. L. Dorset, W. F. Tivol, and J. N. Turner, Acta Crystallogr. A **48**, 562 (1992).

[44] M. J. Buerger, Z. Kristallogr. **109**, 42 (1957).

[45] P. Niggli, *Handbuch der Experimentalphysik*, Vol. 7, Part 1 (Akademische Verlagsgesellschaft, Leipzig, 1928).

[46] M. A. Van Hove, MRS Online Proceedings Library **253**, 471 (1991).

[47] R. Resel, M. Bainschab, A. Pichler, T. Dingemans, C. Simbrunner, J. Stangl, and I. Salzmann, J. Synchrotron Rad. **23**, 729 (2016).

[48] E. F. Semeraro, J. Möller, and T. Narayanan, J. Appl. Cryst. **51**, 706 (2018).

[49] S. Duhm, A. Gerlach, I. Salzmann, B. Bröker, R. L. Johnson, F. Schreiber, and N. Koch, Org. Electron. **9**, 111 (2008).

[50] L. Romaner, D. Nabok, P. Puschnig, E. Zojer, and C. Ambrosch-Draxl, New J. Phys. **11**, 053010 (2009).

[51] X. Shi, R. Q. Zhang, C. Minot, K. Hermann, M. A. Van Hove, W. Wang, and N. Lin, J. Phys. Chem. Lett. **1**, 2974 (2010).

[52] S. R. Kachel, B. P. Klein, J. M. Morbec, M. Schöniger, M. Hutter, M. Schmid, P. Kratzer, B. Meyer, R. Tonner, and J. M. Gottfried, J. Phys. Chem. C **124**, 8257 (2020).

[53] M. Dreher, D. Günder, S. Zörb, and G. Witte, Chem. Mater. **32**, 9034 (2020).

[54] R. Forker, M. Gruenewald, and T. Fritz, Annu. Rep. Prog. Chem. Sect. C **108**, 34 (2012).

[55] R. Forker and T. Fritz, Phys. Chem. Chem. Phys. **11**, 2142 (2009).

[56] F. Sojka and T. Fritz, *LEEDCal 2013, version 4.1* (Fritz & Sojka GbR, Apolda, Germany, 2021).

[57] F. Sojka and T. Fritz, *LEEDLab 2018, version 1.2* (Fritz & Sojka GbR, Apolda, Germany, 2021).

[58] B. Gobaut, P. Orgiani, A. Sambri, E. di Gennaro, C. Aruta, F. Borgatti, V. Lollobrigida, D. Céolin, J.-P. Rueff, R. Ciancio *et al.*, ACS Appl. Mater. Interfaces **9**, 23099 (2017).

[59] D. Knez, G. Dražić, S. K. Chaluvadi, P. Orgiani, S. Fabris, G. Panaccione, G. Rossi, and R. Ciancio, Nano Lett. **20**, 6444 (2020).

[60] R. Ciancio, E. Carlino, G. Rossi, C. Aruta, U. Scotti di Uccio, A. Vittadini, and A. Selloni, Phys. Rev. B **86**, 104110 (2012).

[61] M. E. Sotomayor, B. Levenfeld, A. Varez, and J. Sanz, J. Alloys Compd. **720**, 460 (2017).

[62] S.-I. Kim, H.-J. Choi, G. Lee, C. J. Roh, I. Jung, S. Y. Jung, R. Ning, S. O. Won, H. J. Chang, J. S. Lee *et al.*, Mater. Horiz. **7**, 1552 (2020).

[63] See Supplemental Material at http://link.aps.org/supplemental/10.1103/PhysRevB.104.195402 for our LEED analysis of PTCDA on Ag(111) in comparison to structural data from the literature, which includes Refs. [16,17,64–69].

[64] K. Tojo and J. Mizuguchi, Z. Kristallogr. - New Cryst. Struct. **217**, 253 (2002).

[65] K. Tojo and J. Mizuguchi, Z. Kristallogr. - New Cryst. Struct. **217**, 255 (2002).

[66] A. A. Levin, T. Leisegang, R. Forker, M. Koch, D. C. Meyer, and T. Fritz, Cryst. Res. Technol. **45**, 439 (2010).

[67] M. Möbus, N. Karl, and T. Kobayashi, J. Cryst. Growth **116**, 495 (1992).

[68] C. Ludwig, B. Gompf, W. Glatz, J. Petersen, W. Eisenmenger, M. Möbus, U. Zimmermann, and N. Karl, Z. Phys. B: Condens. Matter **86**, 397 (1992).

[69] L. Kilian, E. Umbach, and M. Sokolowski, Surf. Sci. **573**, 359 (2004).

[70] Q. Wang, A. Franco-Cañellas, P. Ji, C. Bürker, R.-B. Wang, K. Broch, P. K. Thakur, T.-L. Lee, H. Zhang, A. Gerlach, L. Chi, S. Duhm, and F. Schreiber, J. Phys. Chem. C **122**, 9480 (2018).

[71] B. Stadtmüller, T. Sueyoshi, G. Kichin, I. Kröger, S. Soubatch, R. Temirov, F. S. Tautz, and C. Kumpf, Phys. Rev. Lett. **108**, 106103 (2012).

[72] P. Orgiani, A. Perucchi, D. Knez, R. Ciancio, C. Bigi, S. K. Chaluvadi, J. Fujii, I. Vobornik, G. Panaccione, G. Rossi *et al.*, Phys. Rev. Appl. **13**, 044011 (2020).